Mixing and Entrainment in the Red Sea Outflow Plume. Part I: Plume Structure

HARTMUT PETERS AND WILLIAM E. JOHNS

Rosenstiel School of Marine and Atmospheric Science, University of Miami, Miami, Florida

AMY S. BOWER AND DAVID M. FRATANTONI

Woods Hole Oceanographic Institution, Woods Hole, Massachusetts

(Manuscript received 15 September 2003, in final form 2 August 2004)

ABSTRACT

When the salty and heavy water of the Red Sea exits from the Strait of Bab el Mandeb, it continues downslope into the Gulf of Aden mainly along two channels. The 130-km-long "Northern Channel" (NC) is topographically confined and is typically only 5 km wide. In it, the Red Sea plume shows unanticipated patterns of vertical structure, turbulent mixing, and entrainment. Above the seafloor a 25–120-m-thick weakly stratified layer shows little dilution along the channel. Hence this bottom layer undergoes only weak entrainment. In contrast, a 35–285-m-thick interfacial layer shows stronger entrainment and is shown in a companion paper to undergo vigorous turbulent mixing. It is thus the interface that exhibits the bulk of entrainment of the Red Sea plume in the NC. The interfacial layer also carries most of the overall plume transport, increasingly so with downstream distance. The "Southern Channel" (SC) is wider than the NC and is accessed from the latter by a sill about 33 m above the floor of the NC. Entrainment into the bottom layer of the SC is diagnosed to be strong near the entry into the SC such that the near-bottom density and salinity are smaller in the SC than in the NC at the same distance from Bab el Mandeb. In comparison with winter conditions, the authors encountered weaker outflow with shallower equilibration depths during the summer cruise. Bulk Froude numbers computed for the whole plume varied within the range 0.2–1. Local maxima occurred in relatively steep channel sections and coincided with locations of significant entrainment.

1. Introduction

Part of the ventilation of the deep sea is provided by outflows of relatively heavy waters from marginal seas, such as the Mediterranean Sea, the Arctic Ocean, or the Red Sea. There has been great interest in the deep-sea ventilation because it is a crucial element of global climate processes given that the depths of the World Ocean carry the bulk of the heat capacity of the atmosphere–ocean system. Overflowing and outflowing heavy plumes mix with the overlying water and "entrain" the latter, such that potential density decreases along the path of the plume and the transport increases. The terminal depth of outflowing plumes as well as their terminal transport obviously depend on the characteristics of their source water as well as on the strength of entrainment and the characteristics of the entrained water along the plume path. Hence turbulent mixing crucially determines the overall global effect of outflows. Numerical circulation models, for example, cannot possibly simulate the global circulation well without a proper parameterization of mixing in the outflows. Hence there is good reason to explore turbulent mixing in outflows.

We pursue this topic in an analysis of observations taken during the 2001 Red Sea Outflow Experiment (REDSOX). The objectives of REDSOX are to describe the pathways and downstream evolution of the descending outflow plumes of Red Sea water in the western Gulf of Aden, to quantify the processes that control the final depth of the equilibrated Red Sea outflow water, and to identify the transport processes and mechanisms that advect Red Sea outflow water and its properties through the Gulf of Aden and into the Indian Ocean. REDSOX is thus intended to provide the first comprehensive description of the pathways, structure, and variability of the descending outflow plumes from the Red Sea and the equilibrated Red Sea water mass as it enters the western Indian Ocean. This study and a companion paper (Peters and Johns 2005, henceforth referred to as Part II) analyze the descending Red Sea outflow plumes with respect to the relationship of the plume structure on the one hand and mixing and entrainment on the other hand. Herein we discuss velocity and stratification observations, while Part II ana-

Corresponding author address: H. Peters, Rosenstiel School of Marine and Atmospheric Science, University of Miami, Miami, FL 33149.
E-mail: hpeters@rsmas.miami.edu

lyzes the characteristics of the turbulent mixing itself. Below we discuss that the Red Sea outflow water (RSOW) plumes showed a thick interfacial layer that occupied much of the total plume thickness and carried most of the transport and the entrainment. Based on this observation, our emphasis is on the vertical structure of the descending plumes, not on their bulk properties as in previous studies of other outflows, such as, for example, Baringer and Price (1997a,b) or Girton and Sanford (2003).

Until REDSOX, the circulation south of the Strait of Bab el Mandeb had been explored comparatively little, much less than, for example, the outflow from the Mediterranean (e.g., Price and Baringer 1994). Even the seafloor topography was not well known prior to the year 2000. Our two cruises thus had exploratory character in part. In planning REDSOX we relied on the early study by Siedler (1968), moored current-meter and CTD observations in the Strait of Bab el Mandeb and in the outflow channels south of the Strait by Murray and Johns (1997), and the summary of the Red Sea and Persian Gulf outflows by Bower et al. (2000). Of the two "native" water masses of the Indian Ocean, the Persian Gulf and Red Sea Waters, the latter (RSW) is formed in the Red Sea by excess evaporation and enters the Indian Ocean through the 200-m-deep Strait of Bab el Mandeb (BAM) and the Gulf of Aden (Fig. 1). As the RSW flows down from BAM toward the Tadjura Rift, it entrains the overlying Gulf of Aden Water and, according to our findings, equilibrates at a range of depths between 150 and 800 m. The lower part of the mixed Red Sea outflow water has to exit the Tadjura Rift through a narrow gap at its eastern end, and the RSOW is further stirred in the Gulf of Aden by mesoscale eddies (Bower et al. 2002). In the Indian Ocean the RSOW is traceable as a middepth salinity maximum (Rochford 1964; Wyrtki 1971; Beal et al. 2000).

This paper is part of a series in progress of analyses of the Red Sea outflow. The far-field spreading of Red Sea water throughout the Gulf of Aden is examined in Bower et al. (2002) and related to energetic mesoscale eddies spanning the width of the gulf. Last, mixing in the Red Sea outflow is addressed in a numerical modeling study that resolves part of the turbulent motions (Özgökmen et al. 2003).

After this introduction, we outline the REDSOX observations and then provide background information on water masses and temperature–salinity (T–S) distributions, seafloor topography, and seasonality in the Red Sea outflow. Section 4 discusses a simple analytical model that explains why the structure of the Red Sea outflow plumes is robust even though the flow is subject to strong tidal fluctuations at its source. The main results concerning the along-stream depth structure of the descending plumes are presented in section 5, and the paper concludes with a summary and a brief discussion.

2. Observations

The outflow and subsequent spreading of Red Sea water in the Gulf of Aden was observed during two REDSOX cruises in the maximum-outflow winter season and the minimum-outflow summer season. Dates and some statistics of the REDSOX-1 (or RSX-1 for short) on the R/V *Knorr* and the REDSOX-2 (RSX-2) cruise on the R/V *Maurice Ewing* are provided in Table 1, while stations are plotted in Fig. 1. The observations had three main components. (i) High-resolution hydrographic and direct current surveys in the "near field" between the Perim Narrows of Bab el Mandeb Strait and the Tadjura Rift (Fig. 1) were conducted to describe the three-dimensional water property distributions and circulation characteristics. (ii) Direct measurements of turbulent mixing were made to study the bottom stress and vertical transports of mass and momentum in the interface of the descending plumes. (iii) Shipboard surveys of currents and stratification were conducted in the "far field" throughout much of the Gulf of Aden, and acoustically tracked subsurface floats were launched to observe the rates and pathways of Red Sea outflow water spreading. This paper is concerned with the near-field observations, which consist of about 100 casts per cruise as shown in Fig. 1 and listed in Table 1. These casts were taken over an area of approximately 90 km $\times$ 90 km and over the course of 11 and 9 days, respectively, for RSX-1 and RSX-2, and more or less randomly with respect to tidal and longer-term variations in the outflow. In this paper we use only a subset of the near-field observations—stations taken along the axes of the Northern Channel (NC) and Southern Channel (SC; Fig. 1a). Our focus is on the streamwise, distance–depth structure of the plume. The spanwise structure as well as total plume transports integrated over depth and spanwise coordinates is a subject of ongoing investigation.

Stratification and velocity profiles were measured with a package combining a conductivity–temperature–depth probe (CTD), a lowered acoustic Doppler current profiler (LADCP), and a bottle sampler. Our CTD/LADCP package consisted of a SeaBird, Inc., 911Plus CTD and a downward-looking 300-KHz broadband "Workhorse" ADCP from RD Instruments, Inc. Procedures of CTD measurements and their accuracy will be described elsewhere. Turbulent mixing in the interfacial layer of the outflow plumes was observed by extracting overturning scales from the CTD data at their full 24-Hz sampling rates, the topic of Part II. Dedicated microstructure observations of the outflow were not feasible because of the exploratory nature of our experiment and limitations of budget and logistics. For the lowered ADCP we developed measurement and processing routines optimized for observing gravity currents along the seafloor. As a technical matter, these are described in an appendix to Part II along with an

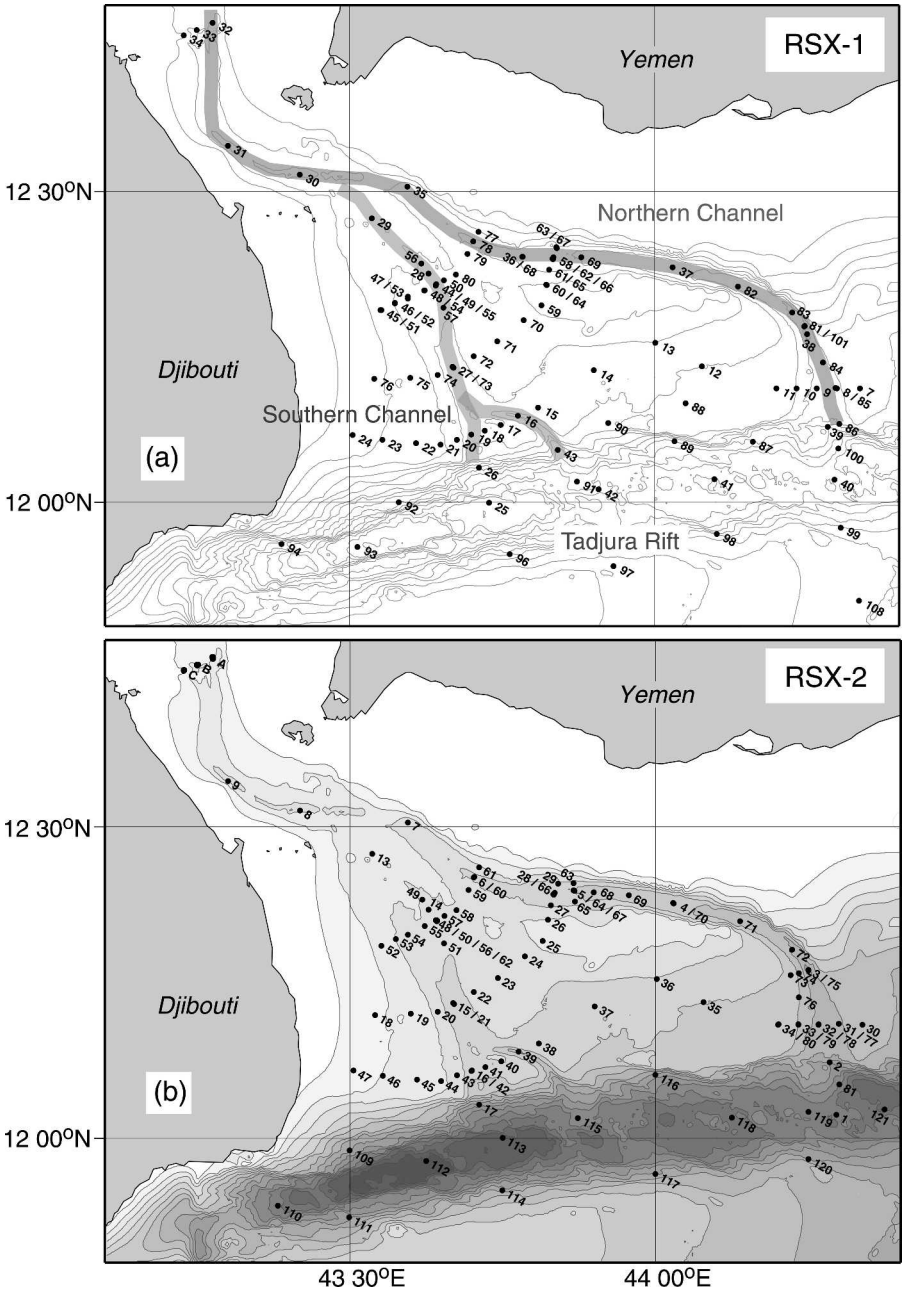

FIG. 1. Station chart from (a) REDSOX-1 (winter) and (b) REDSOX-2 (summer). CTD/LADCP cast numbers are indicated. The seafloor topography in the area of the outflow from the Red Sea between the Strait of Bab el Mandeb in the northwest and the 1200–1600-m-deep Tadjura Rift in the south is also shown. The faint lines in (a) are contours of the water depth at 100-m intervals; shading is added to the contours in (b). The two preferred pathways of the descending plume, the Northern and Southern Channels, are shown in (a). Bab el Mandeb locations A, B, and C in (b) correspond to casts 10–12 and 83–107.

analysis of the uncertainty of the LADCP measurements. In summary, LADCP velocities are uncertain by ± 0.03 m s^{-1}. Following Polzin et al. (2002), we estimated the vertical wavenumber transfer function for the LADCP velocity, finding a 3-db attenuation at a wavelength of 40 m for our setup.

TABLE 1. REDSOX cruises, total number of CTD/LADCP casts, and number in the Red Sea outflow plume area (parentheses).

Cruise	Vessel	Duration (2001)	CTD/LADCP
REDSOX-1	*Knorr*	11 Feb–15 Mar	238 (89)
REDSOX-2	*Maurice Ewing*	21 Aug–12 Sep	227 (108)

We also monitored current profiles with shipboard ADCPs (SADCP), 150-kHz narrowband instruments on both vessels. The SADCP of the *Maurice Ewing*, our ship during the summer cruise, unfortunately had only three functioning beams, making for a geometrically poor setup prone to degradation of the data.

3. Background

a. Seafloor topography

As shown herein, the most dense RSOW flows from BAM down the narrow, typically 5-km wide, Northern Channel to a depth of about 800 m, which is close to the deepest equilibration depths observed in RSOW. This plume is sheltered from effects of rotation along its 120-km-long path (Fig. 1a). Another part of the RSOW flows down the Southern Channel (SC) in which it equilibrates at a shallower depth than in the NC as shown below. The seafloor topography south of the Strait of Bab el Mandeb is unusual in that rather than showing a conventional continental shelf, the terrain slopes down southward to a depth of about 800 m until it drops precipitously into the tectonically active, up to 1600 m deep, Tadjura Rift. The topography along the NC and SC was compiled by S. Swift (2002, personal communication; see also Hébert et al. 2001) from multibeam soundings during our own two cruises on the *Knorr* and the *Maurice Ewing* as well as from an earlier cruise of the *L'Atalante*. The depths along both channel axes are shown in Fig. 2. The typical slope in either channel is approximately ⅓°. A saddle about 33 m above the adjacent NC floor leads from the narrow NC into the wider SC.

b. Seasonality of the outflow and TS environment

The Red Sea outflow differs from other outflows mainly in a pronounced seasonal variability (Murray and Johns 1997), low latitude (12°N) corresponding to relatively small Coriolis parameter, and, more importantly than previously assumed, a number of topographic factors. The Red Sea outflow exhibits a pronounced seasonal variability owing to monsoonal winds. Following Murray and Johns (1997) the transport of RSW at BAM varies from 0.7 Sv (Sv $\equiv 10^6$ m^3 s^{-1}) in winter to 0.05 Sv in summer. Moreover, the waters entrained into the Red Sea outflow also change seasonally. The sill depth at BAM is only 150 m such that the RSW mixes with relatively light water. Preliminary estimates of the total outflow transport during REDSOX-1 amount only to about half of the 2-yr wintertime average from the moored measurements of Murray and Johns (1997). Hence, the plume flow during REDSOX-1 was modest with respect to a longer-term mean.

The detailed *T*–*S* properties of the descending plumes and the overlying waters in the western Gulf of Aden will be analyzed elsewhere. However, a brief summary is included in this paper so that the structure of the plumes can be properly understood. Temperature–salinity distributions in the western Gulf of Aden are complex as illustrated in Fig. 3. In addition to the transport of RSOW along the Northern and Southern Channel, there is a third vein of high-salinity water during winter, which occurs toward the Djibouti coast at a depth of about 150 m. This shallow high-salinity water has equilibrated with its surroundings. It is relevant within this paper only as a property of water that is being entrained into the active outflow plumes in winter. The shallow high-salinity water is absent in summer as shown in Fig. 3. Another major seasonal difference in *T*–*S* properties is that the salinities in the descending plume are much higher in winter. Maximum salinities reach values greater than 39.5 psu in the NC in winter versus only about 38 psu in summer. These differences are related to the seasonal changes in outflow strength from the Red Sea as well as to the vertical structure of the exchange flow in Bab el Mandeb through its effect on the water masses that are available for mixing with the outflow.

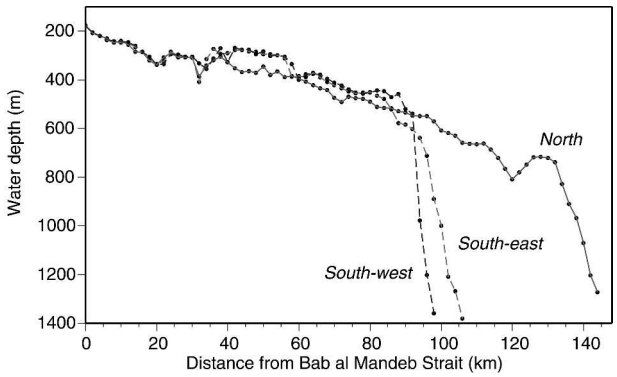

FIG. 2. Depth along the axes of the major channels in the Red Sea outflow area as indicated in Fig. 1a.

4. Source conditions and downstream decay

Our observations of the RSOW plumes are not synoptic with respect to variability on tidal and other time scales, yet a robust structure of the plumes appeared in our initial analysis; Figs. 4a and 4c illustrate the case. The figures depict contours of salinity and current speed in the Northern Channel, which appear rather coherent. We have also contoured other selections of casts repeated at the same or nearby locations of the casts shown in Figs. 4a–d, and the results are similar. Following, we first show that, at its source at BAM, the transport of RSOW underwent strong tidal fluctuations and then introduce a simple analytical model of the downstream decay of such fluctuations. The result is that tidal fluctuations in RSOW transport are damp-

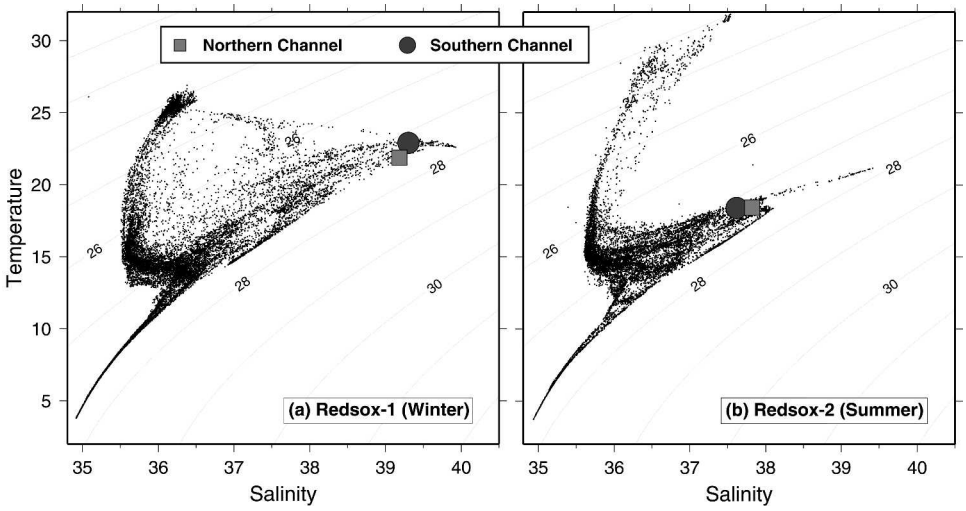

FIG. 3. Temperature–salinity scatterplots from all CTD stations collected in the Bab el Mandeb Strait and western Gulf of Aden during RSX-1 and RSX-2. The large symbols indicate the densest waters issuing into the Gulf of Aden from the northern and southern plumes during each season. The mixed remnants of the winter product waters can be seen as the salinity maximum just underlying the summer product waters.

ened in downstream direction on relatively small space and time scales.

The Strait of Bab el Mandeb exhibits strong tidally oscillating currents with an amplitude of about 0.6 m s^{-1}, an analysis of these tides having been provided by Jarosz (2001). During RSX-2, we made repeated sections across the Perim Narrows in the strait, the north velocity component (v) being shown in Fig. 5c. The local axis of the strait is approximately north–south. Maximum near-bottom salinities, S, varied fairly little, staying above 39 psu even during the minimum outflow season of summer, but the interface above the Red Sea water oscillated vertically with the tide. In consequence, as shown in Fig. 5a, the local transports of volume and salt within the Red Sea water varied tenfold over tidal cycles. These "transports" are simply vertically integrated velocities and velocity times salt, respectively. These are not transports across the entire strait. Here, "salt" means salt concentration times density. The lower limit of integration is the bottom, to which the profiles of v and S were extrapolated. The upper limit of integration is given by either $S < 36.5$ or $v > 0$. Profiles of S and v were extrapolated to the bottom. Transports are local at the deepest spot in the Perim Narrows, the volume transport having a unit of meters squared per second and the salt transport having a unit of kilograms per meter per second.

If such tenfold transport variations were to persist over large distances downstream and downslope from Bab el Mandeb, the structure of the plume as function of depth and distance from the narrows could not possibly be deduced from the kind of nonsynoptic data taken during our cruises. Hence, we proceed to a simple scaling argument why variations in velocity and transport do not propagate far downstream from their source. We depth average the momentum balance across a plume under the influence of reduced gravity and quadratic bottom friction, with interfacial drag and rotation neglected:

$$\frac{du}{dt} = g'\alpha - \frac{c_d u^2}{H}, \tag{1}$$

where u is the depth-averaged plume velocity, reduced gravity is $g' = g\Delta\rho/\rho$, α is the slope of the seafloor, c_d is a drag coefficient, and H is the thickness of the plume. We further simplify the problem by neglecting the spatial dependence in (1) and only consider the time dependence, $u = u(t)$. This amounts to considering (1) to be the equation for the motion of a mass point. With appropriate initial conditions this equation can be readily solved, but it is instructive to normalize it first. The equilibrium velocity for $d/dt \equiv 0$ is $U_e = \sqrt{c_d^{-1} g' \alpha H}$, while the time scale for approaching the equilibrium is $T_e = \sqrt{c_d^{-1} g'^{-1} \alpha^{-1} H}$. Consequently the length scale of approaching equilibrium is simply $X_e = U_e T_e = H/c_d$.

REDSOX conditions prescribe $\alpha = 1/3° \approx 5 \times 10^{-3}$ and $g' \approx 2 \times 10^{-3}$ m s^{-2}. With $c_d = 0.002$ and $H = 100$ m we obtain $U_e = 0.7$ m s^{-1}, a realistic value. With this, we find $T_e = 20$ h and $X_e = 50$ km. Toward interpreting these values correctly, we nondimensionalize (1) with $\tilde{u} = u/U_e$ and $\tilde{t} = t/T_e$ to obtain the normalized equation

$$\frac{d\tilde{u}}{d\tilde{t}} + \tilde{u}^2 = 1. \tag{2}$$

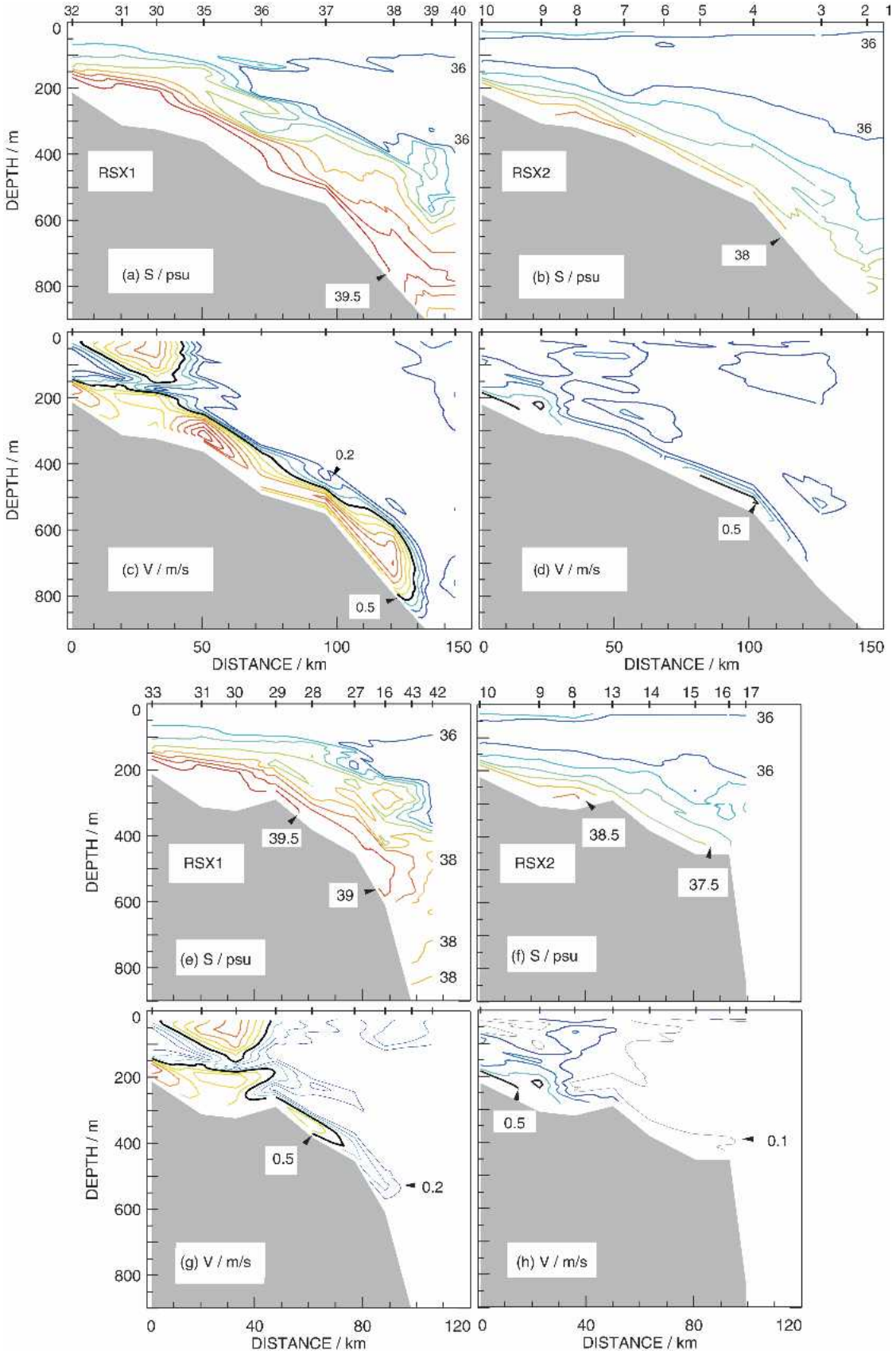
RSX1
(a) S / psu
RSX2
(b) S / psu
(c) V / m/s
(d) V / m/s
(e) S / psu
(f) S / psu
(g) V / m/s
(h) V / m/s
DEPTH / m
DISTANCE / km

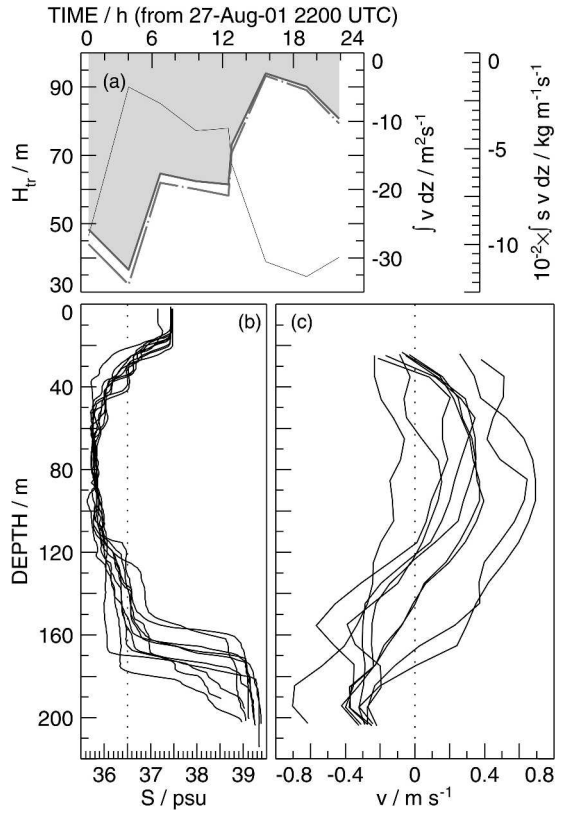

FIG. 5. (a) Transports at the Perim Narrows, Bab el Mandeb Strait; southward (negative) volume transport (solid line + shading), southward salt flux (dash–dotted line), and height above bottom of southward transports (H_{tr}, thin line) as function of time during RSX-2. The salt concentration is $s \approx \rho S/1000$; H_{tr} is the upper limit of vertical integration in computing transports. Profiles of (b) salinity and (c) of the v velocity component at the Perim Narrows, casts taken from 2239 UTC 27 Aug 2001 to 1953 UTC 28 Aug 2001. Water depths at the cast locations ranged from 214 to 220 m.

The solution of (2) is most easily found using the Mathematica program (Wolfram 1999),

$$\tilde{u}(\tilde{t}) = \frac{e^{2\tilde{t}} + e^{C}}{e^{2\tilde{t}} - e^{C}}, \tag{3}$$

where C is an integration constant. Observing that the function $\tilde{u}(\tilde{t})$ in (3) is very similar to $e^{-2\tilde{t}}$, we interpret our results to imply that variations in plume velocity or transport decay downstream on a spatial scale of the order of 25 km and a time scale of the order of 10 h. These small decay scales are consistent with finding a coherent-looking plume structure (Figs. 4a–d) even though the plume source varied significantly on the semidiurnal tidal period and the observations were not synoptic.

5. Plume structure

a. The Northern Channel

As expected for the winter season, the outflow from the Red Sea during REDSOX-1 was strong with maximum plume velocities along the axis of the Northern Channel of 0.6–1.3 m s^{-1} (Fig. 4c). Plume speeds above 0.2 m s^{-1} show swift, active downslope flow in a 100–250-m-thick layer extending 130 km from Bab el Mandeb. The overall plume thickness extends to as far as 300 m off the bottom when elevated salinities greater than 36 psu are considered (Fig. 4a). Near-bottom salinities in the RSOW outflow stayed as high as 39.5 psu as far away as 120 km from BAM (Fig. 4a). The salinity contours in Fig. 4a level out near the lower end of the NC at cast 39, and casts 39 and 40 show a salinity maximum near 800 m, which indicates the equilibration depth of the RSOW plume. Visually, there is little indication of vertical spreading of the plume in the velocity contours. The salinity contours show obvious spreading only toward the lower end of the NC at cast 38.

Figure 4 depicts a selection of nonsynoptic CTD/LADCP casts. In this sense, the contours need to be taken as a means of displaying the data rather than as a snapshot of reality. The contours in Fig. 4, as well as all others shown herein, were computed by means of linear interpolation as a function of normalized depth z/H, where H is the local water depth. Afterward the contours were stretched back to depth z in a procedure that minimizes artifacts of contouring. The seafloor indicated in Fig. 4 solely depicts the water depths at the location of casts, not the full topography. Differing cast

←

FIG. 4. (a)–(d) The Red Sea outflow plume in the Northern Channel from the (left) Strait of Bab el Mandeb to the (right) Tadjura Rift during the winter cruise (REDSOX-1, left) and summer cruise (REDSOX-2, right). The location of the channel is marked in Fig. 1a: (a),(b) salinity and (c),(d) velocity magnitude. Note the lower salinities and lower speeds in the weaker summer outflow when compared with winter conditions. The current direction was approximately constant across the plume at any one location such that the velocity contours represent the local downslope flow except in the upper part of the water column in panels (c) and (d) where inflow into the Red Sea occurred at distances to 50 km from Bab el Mandeb. CTD/LADCP cast numbers are indicated on the top of the graphs. The water depth shown is that at the stations occupied. It is not meant to represent the full channel topography, which is shown in Fig. 2. The contour interval in salinity is 0.5 psu with a range from 36 to 39.5 psu. The color coding runs from blue through green, yellow, and orange to dark red. Contours of speed are at intervals of 0.1 m s^{-1} starting from 0.2 m s^{-1}. The 0.5 m s^{-1} contour is highlighted in black. The 0.1 m s^{-1} contour is suppressed for clarity. (e)–(h) The Red Sea outflow plume in the Southern Channel; (left) (e),(g) winter cruise (REDSOX-1, southeast path); (right) (b),(d) summer cruise (REDSOX-2, southwest path); (e),(f) salinity; (g),(h) velocity magnitude. In comparison with the Northern Channel the plume in the SC had weaker flow and lower salinities. A velocity contour of 0.1 m s^{-1} has been added in (d) in order to make the extension of the plume to the edge of the Tadjura Rift visible. For the two paths of the SC see Figs. 1a and 2.

locations explain, for example, the differences in water depths between Figs. 4a and 4b. The contouring of S and V was reverted to regular depth space where the plume had equilibrated—for example, between casts 39 and 40 in Fig. 4a. We show the velocity magnitude because the direction of the flow tended to be constant through the descending Red Sea plume at any one location (see, e.g., Fig. 6), such that showing V gives a fair view of the local downslope flow in curving channels. Our distance scale has its origin at the Perim Narrows, the location of casts 32–34 in Fig. 1a.

To further describe and illustrate the vertical structure of the Red Sea outflow, we discuss selected individual profiles of salinity (S), temperature (T), velocity magnitude (V) and direction (Φ), squared buoyancy frequency (N^2), and squared shear (V_z^2) with increasing distance from BAM (Fig. 6). Casts 30 (Figs. 6a–c) and 38 (Figs. 6g–i) are typical with respect to the basic division between a mixed or weakly stratified "bottom layer" (BL) that reaches up from the bottom to the velocity maximum and an "interfacial layer" (IL) above this maximum with stronger stratification and large shear. The frequent occurrence of large shear relative to stratification in the IL and in the BL, $V_z^2 > N^2$, corresponds to small Richardson numbers, Ri < 1. A vertical plume structure consisting of BL and thick IL is typical of gravity currents and is seen, for example, in the Mediterranean outflow (Johnson et al. 1994a) or in the Denmark Strait overflow (Girton and Sanford 2003). The distinction between BL and IL is central to our analysis.

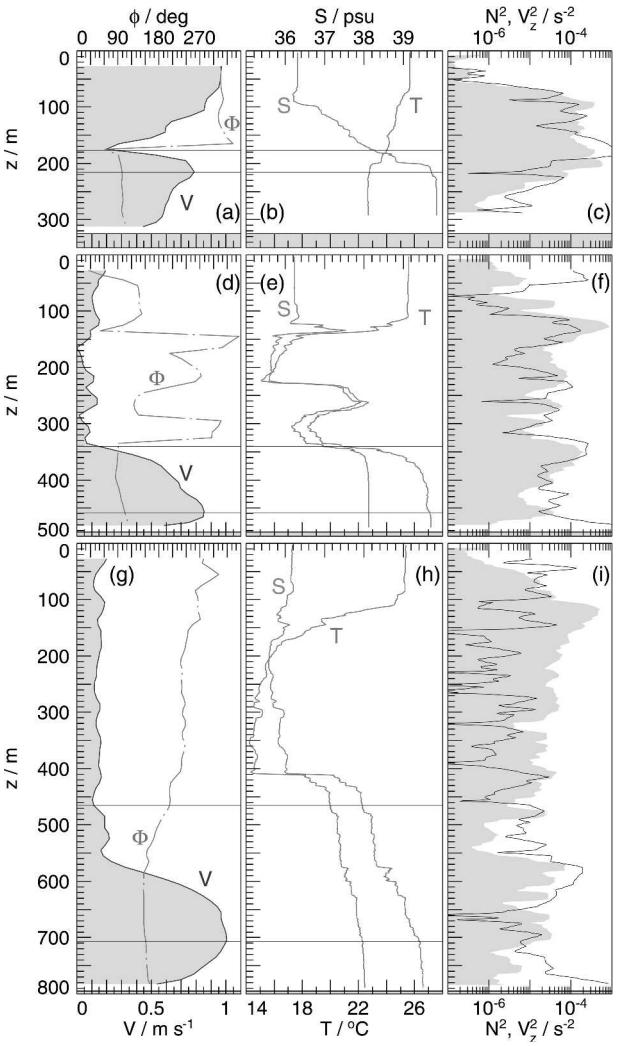

FIG. 6. Velocity and stratification profiles along the Northern Channel, REDSOX-1, cast Nos. (a)–(c) 30, (d)–(f) 36, and (g)–(i) 38. Their locations are marked in Fig. 1a. Distances from BAM are 33, 72, and 121 km, respectively, for casts 30, 36, and 38. Data from these casts are also used in Figs. 4a,c. Local water depths are indicated by shading at the bottom of the panels: (a),(d),(g) speed (shaded) and direction (dash–dotted); (b),(e),(h) temperature (T) and salinity (S) as marked; (c),(f),(i) squared buoyancy frequency (shaded), and squared shear (continuous line).

The relatively large plume velocity at cast 38 appears to be the result of a somewhat steeper-than-average slope upstream of its location as shown in Fig. 2. This cast was taken near an intermediate maximum in the depth of the NC at a distance of 120 km from BAM. Cast 38 displays a much thicker IL than BL, which is typical of the lower reaches of the NC. Cast 30, in the upper reaches of the NC upstream of the branching of NC and SC, had strong inflow into the Red Sea above the outflow from it. Here the IL was thin relative to the BL. In all casts depicted in Fig. 6 the flow direction is seen to be rather constant throughout BL and IL wherever V stayed significantly large. The constancy of Φ in the plume is consistent with a lack of importance of the Coriolis force. It justifies using the velocity magnitude as an indicator of plume flow in a curving channel, especially in the contouring of V in Fig. 4.

Cast 36 in Figs. 6d–f shows intermediate maxima in T and S near 250-m depth in a layer with weak flow. Such lenses of RSOW detached from the active outflow were common in REDSOX, especially in REDSOX-2 when the outflow was weaker and more intermittent than in REDSOX-1, but also during the latter. The T–S diagrams depicted in Fig. 3 illustrate the fact. Note the broad, complex connection between the densest outflow waters and Gulf of Aden waters. Detached RSOW lenses, such as in cast 36, may have been formed at an earlier time or another location. In any case they are evidence of the unsteady nature of the Red Sea outflow. A related feature appears in cast 38 (Figs. 6g–i). High T and S are seen to extend much higher above the seafloor than significant V. An abrupt increase of T and S with increasing depth is seen at 420 m, but large V and near-constant Φ are confined to depths greater than at least 470 m.

To calculate "bulk" properties of the outflow plume and to be able to relate to much of the previous outflow literature we need to formally define the total plume thickness H_p as well as the thicknesses of the BL and IL, H_b and H_i, respectively ($H_p = H_b + H_i$). The top of

the BL is simply taken to be the location of the velocity maximum. In most casts the velocity maximum coincides with the top of the bottom "mixed" layer. Some casts show a more complex structure, however, with relatively weak stratification above the velocity maximum (Figs. 6d–f) or significant structure in T and S below it. Defining the thickness of the IL requires more care and is somewhat fragile and arbitrary because the plume gradually transitions into the background at its top. Formally, we define the top of the IL, and hence the top of the plume, by any one of the conditions $V < 0.075$ m s^{-1}, $|\Delta\Phi| > 45°$ and $S < 36.5$ psu. Here $\Delta\Phi$ is the difference between the average flow direction in the bottom layer and the direction of the local flow. In most cases the top of the plume had both weak flow and a vertically rapid change of flow direction, as seen in Figs. 6a and 6b. Some stations, such as cast 38 in Figs. 6g–i, did not follow this pattern, however, hence the criterion $|\Delta\Phi| > 45°$. The added criterion $S < 36.5$ psu covers the remainder of conditions. As the Red Sea outflow was much weaker during REDSOX-2 than REDSOX 1, we adopted slightly different parameters for the summer cruise, $V < 0.05$ m s^{-1}, $|\Delta\Phi| > 45°$, and $S < 35.7$ psu. Our definition of the vertical extent of the plume is the result of experimentation. The tops of the BL and IL are indicated in Fig. 6 and other profile plots introduced further below. This should allow the reader to critically judge our approach. Herein we define the IL with respect to the structure of an actively flowing plume. We omit from our analysis casts without significant plume flow.

A simple statistical overview of the layer thicknesses of the plumes is given in Table 2, and the data are plotted as a function of distance from BAM in Figs. 7a–d. With respect to the NC during REDSOX-1, it is noteworthy to point out the scatter and lack of obvious trend in H_b and the scatter in H_i. Significant thickening of the IL occurred only toward the lower end of the NC.

The downstream development of the plume in the NC deserves further attention. Above we mention that the BL in the NC maintained very high salinities exceeding 39.5 psu over a distance of 120 km and corresponding to water depths near 800 m. Intuitively, this indicates only weak dilution of the RSW through entrainment. The decrease of the salinity in the bottom layer (S_b) along the NC is shown for all casts at the channel axis along with the near-bottom potential density ($\sigma_{\theta b}$) in Figs. 8a and 8c. A decrease of S_b of about 0.5 psu can be put into perspective by referring to the T–S diagram shown in Fig. 3a. The distance between the densest outflow waters, indicated by the big symbols in Fig. 3a, and the Gulf of Aden waters closest to them in T–S space is about 3 psu in salinity, 6 times as large as the decrease of S_b along the NC. Similarly, we place the decrease in $\sigma_{\theta b}$ along the NC of about 0.35 kg m^{-1} (Fig. 8a) into the context of a reference density profile averaged from casts just outside of the plume area in the Tadjura Rift. Most of the buoyancy anomaly of the BL, depicted in Fig. 7i, is lost in the descent from BAM to the rift not because of entrainment but because of the descent to greater depths and correspondingly larger density of the reference stratification. The difference in the reference σ_θ between 200 m, the water depth at the Perim Narrows, and 800 m, the water depth at the lower end of the NC is 1.4 kg m^{-1} (see Fig. 7i). This is 4 times the drop of $\sigma_{\theta b}$ along the NC. Similar findings have been discussed by Price and Baringer (1994) and Bower et al. (2000).

The preceding numbers attest to relatively weak dilution and, hence, to weak entrainment into the BL of the plume along the NC during REDSOX-1. This weakness of entrainment is surprising given that the swift flow with velocities of 0.6–1.3 m s^{-1} implies vigorous stirring by the bottom shear stress acting along a 120-km path corresponding to a duration of about 2½ days. The strong bottom stirring is reflected in the weak or absent stratification of the bottom layer as shown in Fig. 6. The apparent discrepancy between strong bottom stirring and weak entrainment can be explained by considering the vertical structure and the large thickness of the plume. Figure 8c shows the downstream development of the mean salinity of the entire plume, S_p, which decreased at a rate of approximately twice that of S_b. The figure shows linear fits of salinity versus distance, the fit being forced through the source salinity at BAM of 39.9. The slope of S_b is $-4.1 \times 10^{-3} \pm 1.4 \times 10^{-3}$ psu km^{-1} (correlation coefficient $R = -0.9$), and that of S_p $-1.0 \times 10^{-2} \pm 3.0 \times 10^{-3}$ psu km^{-1} ($R = -0.78$). The scatter in the plume data makes these estimates fairly uncertain but nevertheless indicates twice as much dilution in the plume as a whole as compared with the bottom layer alone. This implies that the mixing and entrainment in the NC were mostly located in the interfacial layer of the plume, a feature further pursued in Part II.

While tidal variations at the plume source in the Strait of Bab el Mandeb do not appear to significantly affect our analysis, there were also longer-term trends in the NC over the course of the REDSOX-1 plume survey. At the lower end of the NC the plume slowed and thinned substantially toward the end of the plume

TABLE 2. Layer thicknesses of the Red Sea outflow plume (m) at the axes of the Northern Channel (NC) and Southern Channel (SC). BL: bottom layer, IL: interfacial layer, P: plume, min: minimum, max: maximum, and n: number of CTD/LADCP casts. Thicknesses of the BL of less than about 15 m are undetectable owing to limitations of the LADCP observations.

	RSX-1				RSX-2			
Quantity	Mean	Min	Max	n	Mean	Min	Max	n
H_b (NC: BL)	59	34	119	21	42	25	88	12
H_i (NC: IL)	102	36	286	21	69	40	116	12
H_p (NC: P)	161	76	344	21	111	65	186	12
H_b (SC: BL)	45	16	119	16	36	16	81	10
H_i (SC: IL)	63	19	146	16	64	21	139	10
H_p (SC: P)	108	49	184	16	100	38	186	10

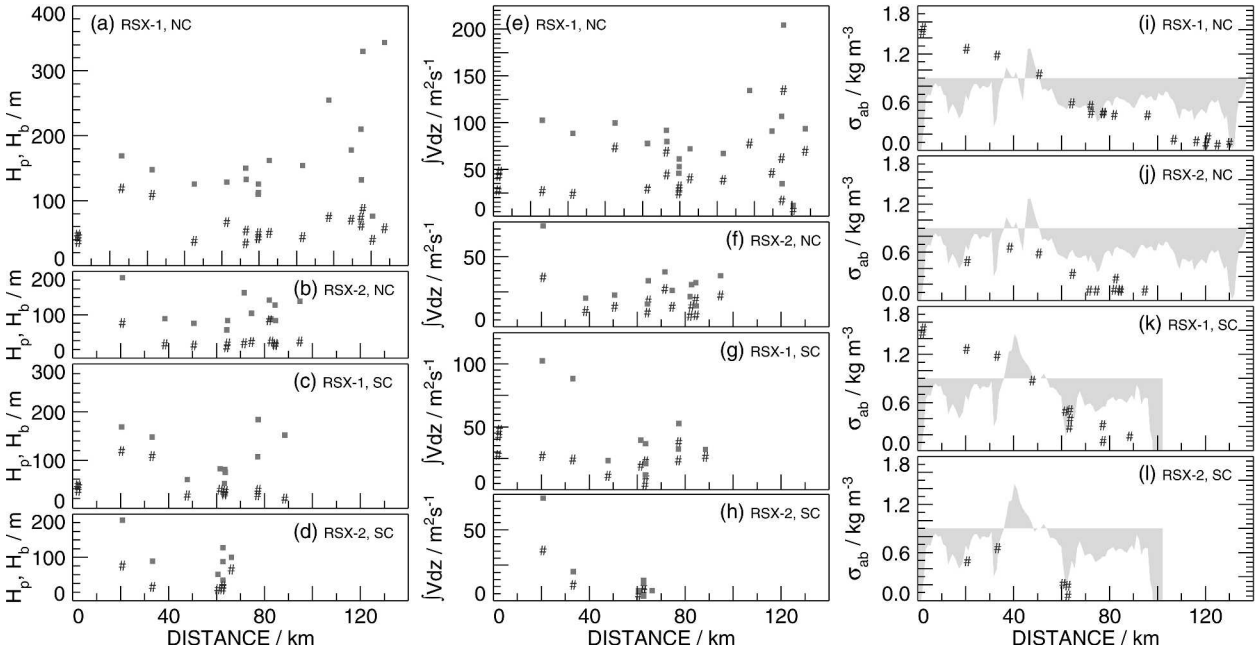

FIG. 7. (a)–(d) Layer thicknesses, (e)–(h) vertically integrated velocities, and (i)–(l) density anomaly relative to Tadjura Rift casts (# symbol) and channel slope on a −0.75° to +0.75° scale; data taken for the two cruises as indicated at the axes of the Northern and Southern Channels. The dots refer to whole plume (V_p, H_p) while the # symbols refer to the bottom layer (V_b, H_b).

survey as shown in Fig. 9. The wide spread of H_b in Fig. 7a near 120-km distance is a consequence of the weakening plume flow shown in Fig. 9. Such fluctuations in the outflow have been more thoroughly characterized by Murray and Johns (1997), who show that they occur on time scales of a few days to a month in relationship to wind forcing.

b. Winter and summer conditions

Figures 4a–d clearly demonstrate the weaker flow and lower salinities of the plume in the NC during REDSOX-2 as compared with REDSOX-1. Such seasonal differences were expected based on the findings of Murray and Johns (1997). Maximum velocities during the summer season shown in Fig. 4d range from 0.2 to 0.5 m s^{-1}, and maximum plume salinities were always below 39 psu. Nevertheless, if the summer plume is taken to be confined within the 0.2 m s^{-1} speed and 38 psu salinity contours, it still extended 110–120 km along the NC. Table 2 and Fig. 7b document the much reduced plume thickness during REDSOX-2 in comparison with the winter case. The weaker summer outflow corresponded to smaller density anomalies (Figs. 7i,j). Examples of velocity and stratification profiles shown in Fig. 10 further convey the observation of comparatively weak flow, thin plume, and reduced salinity in summer as compared with winter. Figure 10 depicts some of the strongest flow observed in the NC during REDSOX-2, which occurred early during the plume survey. At later times there was slower, or altogether negligible, plume flow. Such conditions were to be expected from the observations of Murray and Johns (1997), which indicate that during summer the outflow at BAM can be turned off completely for periods of

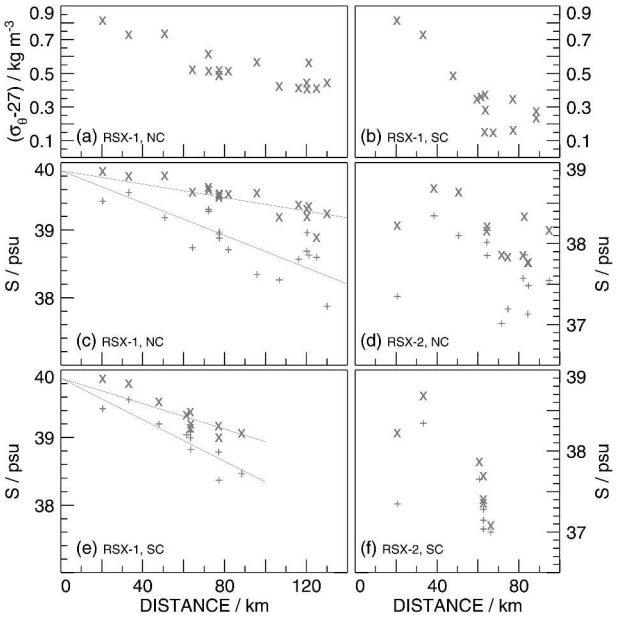

FIG. 8. Near-bottom potential density during REDSOX-1 in (a) the Northern Channel and (b) the Southern Channel. (c)–(f) Salinity as function of along-channel distance for cruises and channels as indicated. Mean bottom layer salinity, ×; mean plume salinity, +.

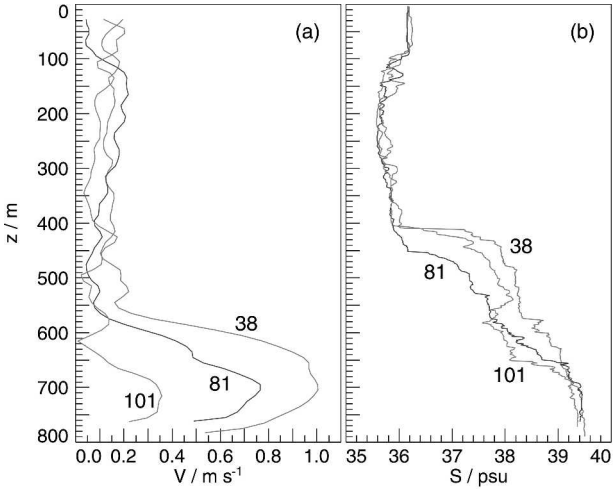

FIG. 9. Variations of (a) velocity magnitude and (b) salinity near the lower end of the Northern Channel, REDSOX-1. The locations of casts 38, 81, and 101 are depicted in Fig. 1a.

days. As a consequence, many casts from REDSOX-2 were not used in this analysis, which is restricted to active plume flow.

As a likely consequence of the unsteadiness of the plume flows during REDSOX-2 the bottom layer salinity S_b and the plume average S_p depicted in Fig. 8d show a confused pattern as compared with REDSOX-1. Consequently, the dilution of the plume along the NC is difficult to diagnose. Figures 4b and 4d do not convey clear evidence of an equilibration depth of the plume. The saline water seen at 750 m at cast 2 could well have been left over from the previous winter. A complete survey of casts from REDSOX-2 shows equilibration at one instance at a depth of 450 m, substantially shallower than in winter. Overall, there possibly was not a single equilibration depth during summer owing to the episodic nature of the outflow.

c. The Southern Channel

During both REDSOX cruises the plume flow in the Southern Channel was slower than in the NC, and salinities were lower (cf. Figs. 4a–d and 4e–h, and Figs. 6 and 11). During REDSOX-1 salinities in the bottom layer of the SC proper, to the right of cast 13 in Fig. 4f, were below 38 psu as compared with being above 39.5 psu in the NC. Peak velocities in the SC during REDSOX-1 were just above 0.6 m s^{-1}, substantially smaller then in the NC. The relatively slow flow in the SC corresponded to smaller density anomalies relative to the Tadjura background (cf. Figs. 7i and 7k). The plume in the SC was also thinner than in the NC as shown in Table 2, Fig. 7c, and in the example cast depicted in Fig. 11. During REDSOX-2 peak velocities in

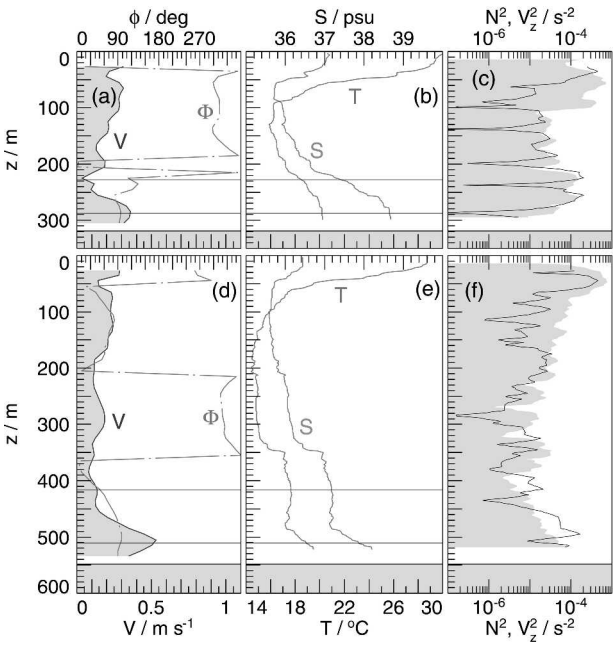

FIG. 10. Velocity and stratification profiles in the Northern Channel, as in Fig. 6, but for REDSOX-2, summer season, cast Nos. (a)–(c) 8 and (d)–(f) 4 (locations: Fig. 1b): (a),(d) speed (shaded) and direction (dash–dotted); (b),(e) temperature (T) and salinity (S) as marked; (c),(f) squared buoyancy frequency (shaded), and squared shear (line).

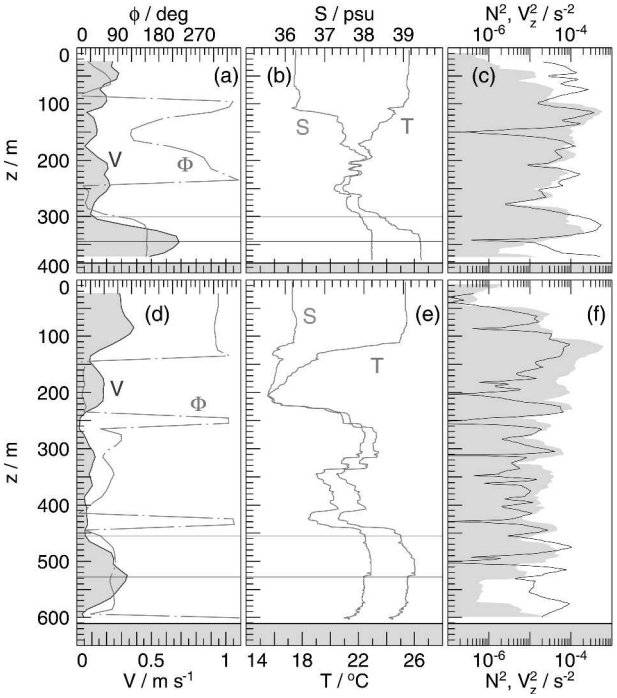

FIG. 11. Velocity and stratification profiles along the Southern Channel, REDSOX-1, casts (a)–(c) 28 and (d)–(f) 16 as indicated in the locater map (Fig. 1a). Local water depths are marked by filling at the bottom of the panels: (a),(d) speed (shaded) and direction (dash–dotted); (b),(e) temperature (T) and salinity (S) as marked; (c),(f) squared buoyancy frequency (shaded), and squared shear (line).

the SC shown in Fig. 4h barely exceeded 0.1 m s^{-1}, and salinities were just above 37.5 psu, demonstrating very weak plume flow. Figures 4f, 4d, and 11 show the most active flow encountered during REDSOX-2. Later during the survey the plume flow was even weaker or ceased altogether.

The Northern and Southern Channels showed different downstream evolutions of salinity and density and different patterns regarding the bottom and interfacial layers. For REDSOX-1, Figs. 8a, 8b, 8d, and 8e show a much stronger downstream decrease of $\sigma_{\theta b}$ and S_b in the SC than in the NC, and hence stronger dilution of the SC plume. An added complication is that temperatures in the bottom layer of the SC were higher than those in the NC. The comparatively low S_b and high T_b combined to a small $\sigma_{\theta b}$ in the SC. The low density resulted in an equilibration depth of the SC plume of about 500 m during REDSOX-1 as seen in Fig. 4e, a depth smaller than the equilibration near 800 m in the NC (Fig. 4a). The equilibrated plume just after leaving the bottom is seen in Figs. 11d, 11e, and 11f at a point where the plume still carried significant momentum. The comparatively small S_b and $\sigma_{\theta b}$ in the SC resulted from strong entrainment into the bottom layer between leaving the main channel at 35-km distance from BAM, over a saddle at 12°30′N, 43°30′E into the SC with the slopes increasing to 0.5° at a distance of 60 km from BAM (Figs. 1, 2, 7k). In comparison with this pronounced drop in BL density and salinity over a fairly short distance in the SC, the decrease of $\sigma_{\theta b}$ and S_b with distance in the NC appears gradual and suggestive of continuous entrainment (Figs. 8a,c,e). The salinity data of Fig. 8e suggest that the difference seen in the NC between weak entrainment into the BL and stronger entrainment into the IL also held in the SC. A linear fit to the SC S_b data yields a salinity slope of $-7.8 \times 10^{-3} \pm 3.5 \times 10^{-3}$ psu km^{-1} while the fit to the plume average S_p has a slope of $-1.3 \times 10^{-2} \pm 4 \times 10^{-3}$ psu km^{-1}.

d. Richardson and Froude numbers

With respect to our interest in mixing and entrainment, it is relevant to look at gradient Richardson numbers in the interfacial layer of the Red Sea plume. The CTD/LADCP casts depicted in Figs. 6, 11, and 10 show both stratification and shear, and thus allow a visual assessment of Ri, $V_z^2 > N^2$ corresponding to Ri < 1. In summary, large V_z^2 relative to N^2 is seen in the bottom layer—that is, below the depth of the velocity maximum—and also in the interfacial layer of the plume above this maximum. It can be shown that Ri $< 1/4$ occurred with significant frequency during both cruises and in both channels, indicating a potential for the occurrence of mixing. In Part II we relate Richardson numbers to observed turbulent overturning and discuss details of the mixing processes. We compute N^2 from potential density with local reference level, sorted into a monotonic sequence such that instabilities related to turbulent overturning are removed and that N^2 is non-negative (Peters et al. 1995). In physical terms, we take the sorted potential density to be an approximation of the "mean" condition that underlies turbulent mixing and gives rise to it. It is important to note that we underestimate shear and correspondingly overestimate Ri owing to the low vertical resolution inherent in LADCP processing (see section 2 and Polzin et al. 2002).

Unlike local gradient Richardson numbers, bulk Richardson numbers do not directly reflect conditions of shear instability and might thus appear to be linked to mixing less directly than Ri. However, analyzing and modeling buoyant flows on the basis of bulk Richardson numbers has a long, successful history marked by, among others, the papers of Ellison and Turner (1959), Turner (1986), and Price et al. (1993). In Part II we also find bulk Richardson numbers to be a useful indicator of mixing and entrainment. Following discussions with J. Price (2003, personal communication), we define the square root of the inverse bulk Richardson number, the bulk Froude number as

$$\mathrm{Fr} \equiv \sqrt{(\rho_0 \delta V^2)\{g \delta\rho [H_b + (1/2)H_i]\}^{-1}}. \qquad (4)$$

Here g is gravity, ρ_0 is a reference density of 1000 kg m^{-3}, δV is the mean speed of the plume, and $\delta\rho$ is its excess density relative to the overlying water, the average over the next 30-m depth above the top of the plume. Taking only one-half of the interface thickness better matches the definitions of $\delta\rho$ and δV than using the full plume thickness H_p. The flow above the Red Sea plume often does not have a simple two-dimensional structure, but tends to be weak except in the upper reaches of the outflow channels (Figs. 4c,d). Therefore we neglect the flow above the plume in the computation of δV. This potentially leads to underestimates of Fr in locations with significant inflow above the Red Sea outflow at distances up to 50 km from BAM, while the simplified calculation of δV is inconsequential otherwise.

Bulk Froude numbers from REDSOX-1 and REDSOX-2 varied between 0.25 and 1 (Fig. 12), being relatively small in comparison with maximum values of over 1 reported by Baringer and Price (1997b) for the Mediterranean outflow. Given that there was mixing and entrainment in the Red Sea plume as shown in Part II, the commonly assumed threshold for active entrainment of Fr = 1 is not compatible with our Fr. The small magnitude of Fr is likely a consequence of a very thick IL relative to the BL. Bulk Fr were originally defined for homogeneous layers with negligibly thin interfaces. For REDSOX-1, Figs. 12a and 12b show relative maxima of Fr at distances just beyond 60 km and near 120 km in the NC and at 50–60-km distance in the SC at locations of relatively large bottom slope. Increases in channel slope will lead to an acceleration of the plume flow and thus to increased Fr. However, this is but one of many processes affecting Fr. Froude numbers be-

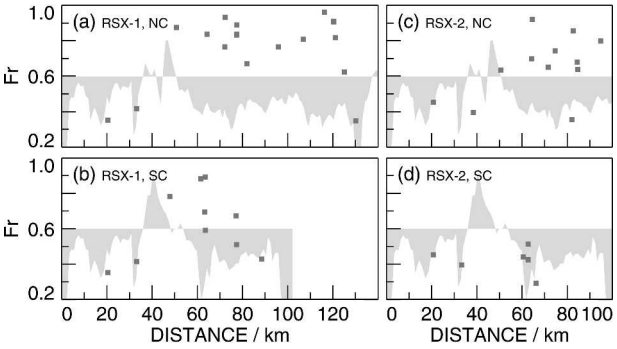

FIG. 12. Bulk Froude numbers as function of distance from Bab el Mandeb for REDSOX-1 and REDSOX-2 and the Northern Channel and Southern Channels as indicated. The channel slope is underlaid with shading on a scale of −0.6° to +0.6°.

came small beyond 120-km distance in the NC and beyond 60 km in the SC, that is toward the end of active plume flow. The maxima of Fr at 50–65-km distance in NC and SC coincide with decreases in the bottom density depicted in Figs. 8a and 8b. In Part II variations of Fr are shown to be correlated with indicators of turbulent mixing in the IL. REDSOX-2 shows sparse Fr data without visually obvious patterns (Figs. 12c,d).

e. Plume transport and the interfacial layer

It is an important aspect of the vertical plume structure that the interfacial layer carried a large part of the total plume transport. As we are using only casts taken at the channel axes herein, we discuss vertically integrated velocities in meters squared per second rather than real transports in meters cubed per second. The flow speed is integrated for the plume layer as a whole, $\mathcal{V}_p = \int_0^{H_p} V\,dz$, and for the bottom layer only, $\mathcal{V}_b = \int_0^{H_b} V\,dz$. Cast data of $\mathcal{V}_b$ and $\mathcal{V}_p$, as well as averages in 50-km distance bin of the latter, are shown for both channels and both cruises in Figs. 7a–d. The largest transports occurred in the NC during REDSOX-1 with typical values of $\mathcal{V}_p$ of 100 $m^2\,s^{-1}$. Relative to these, and at distances greater than 50 km, $\mathcal{V}_p$ was reduced by a factor of 3 in the SC during REDSOX-1 and in the NC during REDSOX-2. In the SC during REDSOX-2 $\mathcal{V}_p$ was a mere 1/7 of the RSX1 NC transport. The relatively small $\mathcal{V}_p$ of REDSOX-2 relative to REDSOX-1 confirm earlier statements about the plume seasonality. It is paralleled by smaller density anomalies relative to a reference density profile (Figs. 7i–l). The small magnitude of $\mathcal{V}_p$ in the SC relative to the NC during both cruises also reflects a weak buoyancy forcing related to a small density anomaly. Following preliminary calculations, the real transport through the SC was about as large as that through the NC as a consequence of the wider cross section of the SC than the NC.

Figures 7e–f show that $\mathcal{V}_b$ tended to be significantly smaller than $\mathcal{V}_p$, indicating that the interfacial layer carried much of the "transport." A closer examination of the ratio $\mathcal{V}_b/\mathcal{V}_p$ is revealing. Distributions of this "transport ratio" for both cruises and in both outflow channels are similar, having median values of about 0.4. The channels are narrower at the bottom and widen with increasing height such that the cross-sectional area associated with the IL is larger than that of the BL. Consequently, a lower bound for the fraction of the true plume transport carried by the IL is 60%. Variations of the transport ratio shown in Fig. 13 turned out to be most interesting. With increasing along-channel distance the relative transport fraction carried by the BL decreased, most noticeably toward the lower ends of the NC and SC. Hence, the fraction of the flow carried by the interfacial layer increased with distance along the outflow channels, a finding attributable to mixing and entrainment.

6. Conclusions

The outflow from the Red Sea into the Gulf of Aden just south of Bab el Mandeb Strait is strongly constrained by the seafloor topography, being largely funneled into two channels.

- The Northern Channel is 130 km long with a typical width of only 5 km. It carried the saltiest and heaviest water.
- The Southern Channel is wider than the NC and shorter. The SC connects to the main channel via a saddle 33 m above the floor of the latter. From this saddle, the plume in the SC consisted of lighter, warmer, and less salty water than in the NC during both winter and summer. The plume flow in the SC was slower than in the NC, roughly corresponding to smaller density anomalies relative to the background stratification in the SC than in the NC.
- The winter season equilibration depth of the plume in the SC was about 500 m as compared with the roughly 800 m in the NC. Summer equilibration depths were nonuniform, tending to be shallower than in winter. Summer plume flows were weak with correspondingly small density anomalies. At times the flow seized completely.

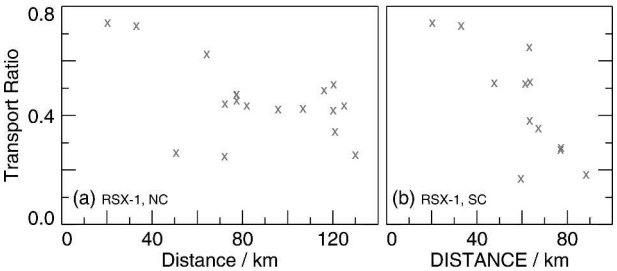

FIG. 13. Ratio of the vertically integrated velocity in the bottom layer to the integral over the entire plume, RSX-1: (a) Northern Channel and (b) Southern Channel.

In the Northern Channel the along-channel depth structure of the plume had intriguing and partly unanticipated properties. We note that, unlike many other locales of outflows, the small width of the channel renders rotational effects insignificant. It also prevents the outflow from spreading laterally, which could possibly increase friction and entrainment.

- We distinguish a weakly stratified "bottom layer" from the overlying "interfacial layer" characterized by stable stratification and high velocity shear. The top of the bottom layer is taken to coincide with the velocity maximum of the plume.
- The thickness of the bottom layer ranged from below 15 to 120 m, that of the interfacial layer from 20 to 285 m, and the maximum total plume thickness was almost 350 m. Over sloping terrain maximum velocities in the plume ranged from 0.6 to 1.3 m s^{-1} in winter.
- At the axis of the channel the interfacial layer carried on average more than one-half of the vertically integrated velocity, implying that the IL carried the bulk of the total plume transport. The fraction of plume transport in the IL increased with distance along the outflow channels in response to mixing and entrainment.
- The bottom layer in the NC showed only weak dilution along a distance of 120 km even though the large plume velocities imply strong stirring at the bottom. During winter, the near-bottom salinity at Bab el Mandeb was about 39.9 psu and stayed above 39.2 psu near the lower end of the NC. Dilution and entrainment were twice as strong in the whole plume as in the bottom layer, which implies that entrainment was dominantly located in the interfacial layer.
- As compared with the strong plume flow in winter we found weak to absent flow during the summer cruise, lower salinities, and smaller equilibration depths.
- The interfacial layer showed large, apparently random variability of local stratification and shear with extensive areas of low Richardson numbers smaller than 1/4. These even occurred in the summer plume.
- Bulk Froude numbers computed for the entire plume varied between 0.25 and 1. The largest Fr occurred in channel sections with a relatively steep slope. The drop in bottom layer density and salinity upon entering the SC was paralleled by large Fr.

In terms of velocity magnitude, vertical scales, and vertical structure the Red Sea outflow plumes show considerable similarity to the Mediterranean outflow as described and analyzed by Johnson et al. (1994a,b) and Baringer and Price (1997a,b). Close to the Strait of Gibraltar the Mediterranean plume shows larger velocities than observed by us but farther west the flow becomes more comparable to the Red Sea plume in the Northern Channel. Previous analyses, such as those by Baringer and Price (1997a,b) and the recent study of the Denmark Strait overflow by Girton and Sanford (2003) have focused on the respective outflow plumes as a whole. Motivated by an interest in the mechanisms, dynamics, and the parameterization of turbulent mixing we emphasize differences between the bottom layer and the overlying interfacial layer of the plume. These differences are probably not unique to the Red Sea outflow. Vertical profiles of the Mediterranean plume provided in Johnson et al. (1994a,b) show great similarity to our observations. Furthermore, Johnson et al. (1994b) noticed that observed turbulent dissipation rates often showed a minimum at the velocity maximum, that is, the top of the BL. Such minima imply a reduction of the vertical turbulent buoyancy flux and, hence, of entrainment into the BL. A general comparison of the Red Sea outflow plume with other outflow is beyond the present scope, and thus we refrain from further comments on similarities and differences to other outflow. Nevertheless it remains intriguing to explore how different the Denmark Strait and the Red Sea plumes are considering how the differences in topographic conditions favor or disfavor the Coriolis force.

How important is it to make a distinction between the bottom layer and the interfacial layer when treating plume dynamics? Bulk plume models are great tools for investigating and understanding plume dynamics. However, they may not be an adequate tool for parameterizing mixing in numerical circulation models with significant vertical resolution of the plume flow. The weakness of entrainment in the bottom layer of the Northern Channel has the consequence of transporting relatively undiluted Red Sea water to comparatively great depth, while the presence of a thick IL causes a wide vertical spread of Red Sea outflow water. Hence the vertical structure of the Red Sea plume has significant consequences for the further spreading of Red Sea water.

Acknowledgments. The Red Sea Outflow Experiment was funded by the National Science Foundation under Contracts OCE-9819506 and OCE-9818464. Additional support was provided to the "Climate Process Team Gravity Currents" under OCE-0336799. The good work of the masters and crews of the R/V *Knorr* and the R/V *Maurice Ewing* is gratefully acknowledged. Numerous members of the science parties on the REDSOX-1 and REDSOX-2 cruises greatly contributed to the work reported herein. We are especially indebted to RSMAS technicians Mark Graham and Robert Jones; to Rainer Zantopp, who processed the CTD data; and to Silvia Matt, who assisted with reducing of the LADCP data. In developing routines for LADCP processing we benefited greatly from material provided by, and discussions with Martin Visbeck. The bathymetric data from the Gulf of Aden, including data from the *L'Atalante* generously provided by Philippe Huchon, were worked up by Stephen Swift. We sincerely thank both of them. We greatly benefited from

further hints by and discussions with Eric Firing, Tamay Özgökmen, Jim Price, and James Girton. As usual, Linda Peters was the able coach on style and diction. Clearance to work in the territorial waters of Djibouti, Eritrea, and Yemen is gratefully acknowledged.

REFERENCES

Baringer, M., and J. F. Price, 1997a: Mixing and spreading of the Mediterranean outflow. *J. Phys. Oceanogr.,* **27,** 1654–1677.

——, and ——, 1997b: Momentum and energy balance of the Mediterranean outflow. *J. Phys. Oceanogr.,* **27,** 1678–1692.

Beal, L. M., A. Ffield, and A. L. Gordon, 2000: The spreading of Red Sea overflow waters in the Indian Ocean. *J. Geophys. Res.,* **105,** 8549–8564.

Bower, A. S., H. D. Hunt, and J. F. Price, 2000: Character and dynamics of the Red Sea and Persian Gulf outflows. *J. Geophys. Res.,* **105,** 6387–6414.

——, D. M. Fratantoni, W. E. Johns, and H. Peters, 2002: Gulf of Aden eddies and their impact on Red Sea water. *Geophys. Res. Lett.,* **29,** 2025, doi:10.1029/2002GL015342.

Ellison, T. H., and J. S. Turner, 1959: Turbulent entrainment in stratified flows. *J. Fluid Mech.,* **6,** 423–448.

Girton, J. B., and T. B. Sanford, 2003: Descent and modification of the overflow plume in the Denmark Strait. *J. Phys. Oceanogr.,* **33,** 1351–1364.

Hébert, H., C. Deplus, P. Huchon, K. Khanbari, and L. Audin, 2001: Lithosphere structure of a nascent spreading ridge inferred from gravity data: The western Gulf of Aden. *J. Geophys. Res.,* **106** (B11), 26 345–26 363.

Jarosz, E., 2001: Tidal dynamics in the Bab el Mandeb Strait. Ph.D. thesis, Louisiana State University, 153 pp.

Johnson, G. C., R. Lueck, and T. B. Sanford, 1994a: Stress on the Mediterranean outflow plume: Part II. Turbulent dissipation and shear measurements. *J. Phys. Oceanogr.,* **24,** 2084–2092.

——, T. B. Sanford, and M. O. Baringer, 1994b: Stress on the Mediterranean outflow plume: Part I. Velocity and water property measurements. *J. Phys. Oceanogr.,* **24,** 2072–2083.

Murray, S. P., and W. E. Johns, 1997: Direct observations of seasonal exchange through the Bab el Mandeb Strait. *Geophys. Res. Lett.,* **24,** 2557–2560.

Özgökmen, T. M., W. E. Johns, H. Peters, and S. Matt, 2003: Turbulent mixing in the Red Sea outflow plume from a high-resolution nonhydrostatic model. *J. Phys. Oceanogr.,* **33,** 1846–1869.

Peters, G. C., and M. O. Johns, 2005: Mixing and entrainment in the Red Sea outflow plume. Part II: Turbulence characteristics. *J. Phys. Oceanogr.,* **35,** 584–600.

Peters, H., M. C. Gregg, and T. B. Sanford, 1995: Detail and scaling of turbulent overturns in the Pacific Equatorial Undercurrent. *J. Geophys. Res.*, **100**, 18 349–18 368.

Polzin, K., E. Kunze, J. Hummon, and E. Firing, 2002: The finescale response of lowered ADCP velocity profiles. *J. Atmos. Oceanic Technol.,* **19,** 205–224.

Price, J. F., and M. O'Neil Baringer, 1994: Outflows and deep water production by marginal seas. *Progress in Oceanography,* Vol. 33, Pergamon, 161–200.

——, and Coauthors, 1993: Mediterranean outflow mixing dynamics. *Science,* **259,** 1277–1282.

Rochford, D. J., 1964: Salinity maxima in the upper 1000 metres of the north Indian Ocean. *Aust. J. Mar. Freshw. Res.,* **15,** 1–24.

Siedler, G., 1968: Schichtungs und Bewegungsverhältnisse am Südausgang des Roten Meeres. *"Meteor" Forsch.-Ergebn. Reihe,* **A** (4), 1–67.

Turner, J. S., 1986: Turbulent entrainment: The development of the entrainment assumption, and its applications to geophysical flows. *J. Fluid Mech.,* **173,** 431–471.

Wolfram, S., 1999: *The Mathematica Book*. 4th ed. Wolfram Media/Cambridge University Press, 1470 pp.

Wyrtki, K., 1971: *Oceanographic Atlas of the International Indian Ocean Expedition.* National Science Foundation, 531 pp.